

A New Model of the Madden-Julian Oscillation

David J. Raymond

Physics Department and Geophysical Research Center

New Mexico Tech

Socorro, NM 87801

email: raymond@kestrel.nmt.edu

Submitted to *Journal of the Atmospheric Sciences*

Revised Version

October 30, 2005

Abstract

A new model of the Madden-Julian oscillation (MJO) is presented. Cloud-radiation interactions in this model make the tropical atmosphere susceptible to large-scale radiative-convective overturning. The modeled MJO takes the form of such an instability, though its behavior is substantially modified by the effects of surface heat flux variability. The dynamics of the disturbance in the model are quasi-balanced, in the sense that the low-level flow in the disturbance is more associated with the vorticity than with the divergence. The cumulus parameterization used in the model allows a lag of several days to exist between the strongest surface heat flux into a column and the development of heavy precipitation in that column. This lag plays a key role in model dynamics.

1 Introduction

Explaining the Madden-Julian oscillation (MJO; Madden and Julian, 1971, 1972, 1994) has become a “holy grail” in the quest to understand tropical atmospheric dynamics. This paper is a contribution to the search.

Hayashi and Golder (1993) reviewed theoretical and modeling work on the MJO up to the date of their paper. Most recent work characterizes the MJO as some form of mixed Kelvin-Rossby mode, with the two components being coupled together by diabatic or frictional effects (Hendon, 1988; Wang and Rui, 1990; Salby, Garcia, and Hendon, 1994; Moskowitz and Bretherton, 2000).

Wheeler and Kiladis (1999) presented a plot of the variance of near-equatorial outgoing longwave radiation (OLR) as a function of frequency (ω) and zonal wavenumber (k). After removing a red noise background, these plots showed all of the equatorial wave modes predicted by Matsuno (1966) and Lindzen (1967). In addition, the MJO appeared as a distinct mode separated from the Kelvin mode, with a fixed frequency independent of wavenumber, i. e.,

$$\omega = \Omega, \tag{1}$$

where $\Omega \approx 2\pi/(40 \text{ d})$ is a constant. This contrasts with the Kelvin wave dispersion relation $\omega = ck$, where $c \approx 10 - 25 \text{ m s}^{-1}$ is the phase speed of the observed Kelvin waves, and suggests that the MJO is actually a wave packet with zero group velocity u_g :

$$u_g = \frac{d\omega}{dk} = 0. \tag{2}$$

Observations that the eastward-moving MJO wave essentially disappears in OLR between the eastern Pacific and the western Indian Ocean (e. g., Salby and Hendon, 1994; Hendon and Salby, 1994) would seem to support the view that the convective pattern associated with the MJO (as represented by the OLR) is a stationary wave packet with eastward-moving phase waves confined primarily to the eastern Indian and western Pacific oceans, as implied by the analysis of Wheeler and Kiladis (1999).

It is instructive to examine unfiltered plots of OLR in specific latitude ranges, even though many sophisticated statistical analyses of this data set have been made. Figures

1 - 3 respectively show longitude-time plots of daily OLR (Liebmann and Smith, 1996) from 1 July 1996 to 20 December 1997 over the latitude ranges $7.5^\circ \text{ S} - 7.5^\circ \text{ N}$, $7.5^\circ \text{ N} - 12.5^\circ \text{ N}$, and $12.5^\circ \text{ S} - 7.5^\circ \text{ S}$. Let us refer to these as the *equatorial band*, the *north ITCZ band*, and the *south ITCZ band*. (ITCZ is the intertropical convergence zone.) The strong 1997-1998 el Niño begins at about the middle of this time period.

The most obvious feature of the equatorial band is the deep convection over the west Pacific and east Indian ocean warm pool. This appears between 60° E and 180° E during normal years, but shifts eastward during el Niño, as figure 1 shows. The modulation of this convection by the $\approx 5 \text{ m s}^{-1}$ eastward movement of the MJO modes is quite obvious in figure 1. These waves appear to die out east of 180° E in normal years. However, during el Niño, east Pacific equatorial waters are warm and OLR signals continue eastward of the main convective region, albeit at somewhat higher speeds. These are presumably the modes identified by Wheeler and Kiladis (1999) as Kelvin waves. These waves repeat at frequencies much higher than the typical MJO frequency of $\approx (40 \text{ d})^{-1}$, as inspection of figure 1 near 240° E after day 420 shows.

Close examination of figure 1 shows that there are westward as well as eastward moving OLR signatures. These tend to be small in scale and to occur within the envelope of the larger scale MJO wave, as indicated by Lau, Nakazawa, and Sui (1991). Westward-moving disturbances are much more obvious in the north and south ITCZ bands, as shown in figures 2 and 3.

Comparison of the equatorial and ITCZ bands shows that the MJO is most evident in the ITCZ band in the summer hemisphere, and is almost absent in the winter ITCZ band. Thus, MJO convection follows the sun, probably as a consequence of the annual latitudinal movement of the sea surface temperature (SST) maximum.

Hendon and Salby (1994) showed that the MJO has a mean low-level structure over the warm pool consisting of an elongated westerly jet many thousands of kilometers in length on or near the equator, flanked near the east end of the jet by cyclonic vortices in both hemispheres. The vortices are rather large in scale, extending to $\pm 45^\circ$ of latitude. According to Hendon and Salby (1994), when the MJO wave exits the warm pool,

it accelerates to typically 10 m s^{-1} and the vortices become less evident. However, inspection of figure 1 suggests that the “MJO” outside the warm pool may actually be the Kelvin waves of Wheeler and Kiladis (1999). Since Kelvin waves have a quite different dispersion relation than the MJO in their results, perhaps there are two distinct phenomena occurring.

Recently there has been an effort to rethink the problem of the forcing of deep convection in the tropics (Emanuel and Raymond, 1993; Emanuel, Neelin, and Bretherton, 1994; Raymond, 1995; Smith, 1997). The notion that thermodynamics rather dynamics plays the more important role in convective forcing on large scales has been gaining ground.

In retrospect, the work of Neelin and Held (1987) becomes particularly enlightening. In this work the authors showed that deep convective activity in the tropics is directly proportional to the net energy input into the troposphere from surface fluxes and radiation, and inversely proportional to a quantity the authors called the *gross moist stability* (GMS). The GMS is proportional to the net export of energy per unit of mass flowing through the deep convective region.

The paper of Neelin and Held (1987) is based on a time-independent analysis of the moist static energy budget in the troposphere. The assumption of time-independence means that their analysis is not prognostic for time-varying situations. However, Raymond (2000b) showed that this restriction could be lifted if it is reasonably assumed that clouds in higher humidity environments precipitate more heavily. In this case a rapid increase in thermodynamic forcing (i. e., in the net energy convergence in the troposphere from surface and tropopause enthalpy fluxes) results first in a moistening of the troposphere, followed after a lag of possibly many days by an increase in precipitation.

The purpose of this paper is to see how this hypothesis for deep convective forcing might play out in the tropical atmosphere using the model of Raymond and Torres (1998), as corrected and enhanced by Raymond (2000a). This model uses updated versions of the diabatic parameterizations of Raymond (1994). As we shall demonstrate, these diabatic parameterizations closely follow the behavior outlined by Raymond

(2000b).

We emphasize here that the results of Raymond and Torres (1998) are obsolete for two main reasons:

1. Shortly after publication, we discovered a vertical interpolation error in the model which located the heating half a grid interval away from where it should have been applied. This had particularly strong consequences at the surface. When this error was corrected, the resulting modes were no longer unstable, thus removing them from consideration as an explanation for superclusters or the MJO. This result was reported by Raymond (2000a).
2. Cloud-radiation interactions, which were not included by Raymond and Torres (1998), were shown to be of potentially great significance to large-scale motions in the tropics (Slingo and Slingo, 1988, 1991; Randall, Harshvardhan, Dazlich, and Corsetti, 1989; Sherwood, Ramanathan, Barnett, Tyree, and Roeckner, 1994; Raymond, 2000a). Raymond (2000a) showed that cloud-radiation interactions might be sufficient to cause the development of an off-equatorial Hadley circulation even in the absence of latitudinal sea surface temperature (SST) or solar shortwave radiation gradients. Thus, the Raymond-Torres results are unlikely to be representative of actual tropical behavior for this reason as well.

In this paper a series of three-dimensional equatorial beta-plane calculations with fixed SST patterns is made. When cloud-radiation interactions are turned on, large-scale disturbances develop even when the SST is uniform. Without these interactions, no instability exists. Thus cloud-radiation interactions are central to the large scale dynamics of the tropical troposphere in this model.

When simplified SST distributions similar to observed distributions are introduced, the resulting disturbances look and behave very much like the observed MJO. In particular, a wavenumber-one equatorial disturbance moves to the east at about 5 m s^{-1} when there is an equatorial SST maximum. This disturbance exhibits the low-level cyclonic gyres evident in the observations. When an equatorial warm pool is added to the SST

pattern, eastward-moving disturbances are periodically emitted from the warm pool region. The convection in these disturbances dissipates shortly after they move out of the warm pool, in agreement with MJO observations.

Analysis of the simulations indicates that the modeled disturbances do not exhibit Kelvin wave dynamics. Instead, they are slow manifold disturbances which operate in accordance with the weak temperature gradient approximation of Sobel and Bretherton (2000) and Sobel, Nilsson, and Polvani (2001). We demonstrate this using a variety of diagnostic techniques.

Section 2 briefly describes the model. The MJO simulations are presented in section 3. The factors underlying model behavior are investigated in section 4, and conclusions are presented in section 5.

2 Model

The model of Raymond and Torres (1988) as modified by Raymond (2000a) is used here, with two additional modifications:

1. Stratiform rain generation is not allowed if $\Gamma_e \equiv \partial\theta_e/\partial z < 2 \text{ K km}^{-1}$, where θ_e is the equivalent potential temperature, and is fully turned on when $\Gamma_e > 4 \text{ K km}^{-1}$.
2. The horizontal wind components are defined at vertical cell centers rather than cell edges.

The first of the above conditions is based on the hypothesis that true saturation (and hence stratiform rain generation) cannot occur in an environment in which $\Gamma_e < 0$. Apparent saturation on the grid scale in such conditions is interpreted as the result of averaging over an unsaturated environment pierced by saturated convective cores. Since the cumulus parameterization is dealing with these cores, it would be a mistake to treat the environment there as saturated. Imposition of this condition eliminates spurious moist convective instability on the grid scale.

Constant	Value	Meaning
δ_h	0.005	horizontal smoothing parameter
γ	2	horizontal deformation parameter
ν	0.0001 ks ⁻¹	vertical smoothing rate
w_c	0.05 m s ⁻¹	convective mixing velocity
λ_s	0.1 ks ⁻¹	stratiform rain rate
λ_p	0.00002 ks ⁻¹	convective rain rate
λ_e	200 ks ⁻¹	evaporation rate
C_D	0.001	drag coefficient
W	3 m s ⁻¹	gustiness correction
κ_c	75000 m ³ kg ⁻¹ km ⁻¹	cloud radiation absorption parameter

Table 1: Values of adjustable model constants used in this paper. See Raymond (2000a) for their definitions.

The second change was made because defining horizontal velocities on vertical grid edges results in spurious small scale oscillations in the vertical structure of the horizontal wind. These oscillations disappear when the above change is made.

The model is run on a domain 40000 km in the zonal direction and 10000 km in the meridional direction. The horizontal grid size is 250 km by 250 km. The model top is set to 60 hPa and 30 layers equally spaced in the vertical coordinate $\sigma = (\theta - \theta_B)/(\theta_T - \theta_B)$ are used. (The parameter θ is the potential temperature and the subscripts indicate values at the top (T) and bottom (B) of the domain.) North and south boundaries are rigid walls with free-slip conditions, while the model is periodic in the east-west direction. The model is centered in the north-south direction on the equator. There is no land in the model and the SST is specified. The time step is taken to be 0.25 ks and the model is typically run for 10000 ks (about 116 d), occasionally for longer or shorter periods.

Table 1 gives the values of adjustable constants used in the model, as defined by Raymond (2000a). Compared to that paper, the horizontal deformation parameter γ ,

the vertical mixing rate ν , the drag coefficient C_D , and the cloud absorption coefficient κ_c are all reduced. The mixing constants are reduced because there is no longer need to suppress the small scale vertical oscillations in the horizontal wind. The drag coefficient is set to $C_D = 0.001$, which is its approximate observed value. The previous larger value of 0.002 was needed to keep sea-air temperature differences from becoming too large. However, inclusion of cloud-radiation interactions has eliminated this problem. Finally, the cloud radiation absorption coefficient is set to be consistent with an effective cloud drop radius of 10 μm in the context of the simple radiative model used here (see Raymond and Zeng, 2000).

The parameters controlling cloud-radiation interactions are largely a matter of guesswork at this point. However, the current selections result in cloud radiative effects roughly consistent with the diagnostic calculations of Johnson and Ciesielski (2000) for the west Pacific warm pool.

Curiously, the above-mentioned changes in the values of C_D and κ_c cause the zonally symmetric Hadley circulation instability of Raymond (2000a) to vanish, indicating that this instability is marginal for realistic parameter values. However, the zonally symmetric case turns out to be more stable than the fully three-dimensional case, as we shall show.

3 Overview of simulations

In this section we briefly present the results of three different simulations with differing spatial distributions of SST. The first case has uniform SST. The second has a zonally symmetric SST distribution which approximates the observed distribution within about 2500 km of the equator. The third adds an equatorial warm pool to the SST distribution in the second simulation.

3.1 Uniform SST

In this section we examine the results from a simulation in which the SST is set uniformly to 300 K over the domain. The atmosphere is first run to radiative-convective

equilibrium at the specified SST with the effective windspeed equal to W . Convection is initiated by a total water mixing ratio anomaly of the form

$$r'_t(x, y, z) = Hr_{t0}(z)F(d)(z/z_s) \exp(1 - z/z_s), \quad (3)$$

where $r_0(z)$ is the radiative-convective equilibrium mixing ratio profile of total water, $z_s = 5$ km, and

$$F(d) = \begin{cases} \{1 + \cos(\pi d)\}/2, & d \leq 1 \\ 0, & d > 1 \end{cases}, \quad (4)$$

where $d^2 = (x - x_0)^2/x_s^2 + (y - y_0)^2/y_s^2$. The constants are set as follows: $x_0 = 20000$ km (centered in the x domain); $y_0 = 5500$ km (500 km north of equator); $x_s = 400$ km; $y_s = 2000$ km; $H = 0.8$.

The initial disturbance is offset north of the equator to see whether an equatorially symmetric disturbance does or does not develop subsequently. It turns out that the initial disturbance amplifies and actually moves farther off the equator, with a maximum precipitation rate developing near $y = 5750$ km. Figure 4 shows the precipitation rate resulting from the disturbance at this latitude. Note that the disturbance drifts eastward at about 2 m s^{-1} .

The general form of this disturbance is independent of the initial conditions. Initialization with random fluctuations in the mixing ratio field yields quite similar results after a period of self-organization.

The low-level wind and rainfall patterns in the disturbance at $t = 6000$ ks are shown in figure 5. They are characteristic of the structure over most of the integration period. A strong low-level westerly jet, centered just north of the equator and bounded on the north and south by gyres, feeds the region of maximum precipitation. The jet maximum is in excess of 15 m s^{-1} and the precipitation maximum is greater than 20 mm d^{-1} . The return flow around the north side of the northern gyre comes close to the north wall of the model, where it appears to stimulate a wall mode. This mode is obviously an artifact of the presence of the wall, but is highly trapped so that it is unlikely to have much influence on the circulation far from the wall.

3.2 Zonally symmetric SST

The meridional SST distribution used in this simulation is illustrated in figure 6. It approximates the observed annual and zonal mean SST distribution (Peixoto and Oort, 1992) and is given by the equation

$$T_{SS}(y) = T_0 + \Delta T[4F(\eta) - F(2\eta)]/3 \quad (5)$$

where $T_0 = 295$ K, $\Delta T = 6$ K, F is defined by (4), and $\eta = (y - y_{eq})/y_{wid}$. The parameter $y_{eq} = 5000$ km locates the equator, while $y_{wid} = 4000$ km defines the half-width of the SST peak, which is centered on the equator. The function $T_{SS}(y)$ is designed so that d^2T_{SS}/dy^2 is zero on the equator. The near-equatorial variation in the SST value from its value at the equator thus depends on the distance from the equator to the fourth power rather than the second power. To the extent that the SST reflects the air temperature, this implies zero geostrophic vertical wind shear in the atmosphere over the equator.

The simulation in this case is initialized with random fluctuations in the tropospheric humidity. The resulting disturbance self-organizes out of this initial distribution and moves to the east at about 5 m s^{-1} with a wavenumber one structure. Figure 7 shows the pattern of rainfall along the equator as a function of longitude and time for this case.

Figure 8 shows a snapshot of the rainfall and the horizontal winds averaged over the lowest 4 km at 10000 ks. The disturbance is equatorially symmetric aside from small perturbations arising from the random initialization. The wind along the equator is calm ahead of the disturbance, with strong westerly flow overlapping and to the west of the rainfall. Cyclonic gyres are seen in both hemispheres, with structure quite similar to that described by Hendon and Salby (1994).

3.3 Warm pool

Figure 9 shows the assumed distribution of SST for the warm pool simulation. This consists of the SST distribution used in the zonally symmetric case plus a superimposed warm pool perturbation of the form

$$\Delta T = \Delta T_0 F(d) \quad (6)$$

where $d = [(x - x_0)^2/x_s^2 + (y - y_0)^2/y_s^2]^{1/2}$ and where $\Delta T_0 = 3$ K, $x_s = 12000$ km, and $y_s = 2000$ km. The values of x_0 and y_0 are set so as to place the warm pool on the equator in the center of the domain. The simulation is initialized with a random distribution of humidity perturbations, so as to facilitate the development of any possible equatorially asymmetric instabilities that wouldn't be activated by the equatorially symmetric SST distribution. As it turns out, equatorial asymmetry doesn't develop in the simulation under these conditions.

The rainfall rate on the equator as a function of longitude and time for the warm pool simulation is shown in figure 10. Note how disturbances are periodically generated over the west end of the warm pool. They propagate to the east at a somewhat ill-defined speed in the range $4 - 7$ m s⁻¹ and dissipate near the east edge of the warm pool. The repetition period is about 2300 ks or 27 d and the individual disturbances look much like those which occur in the equatorially symmetric case (see figure 8).

3.4 Assessment of simulations

The above simulations are similar in that they all exhibit a large, off-equatorial cyclonic gyre at low levels bounded on the equatorial side by a strong ($10 - 15$ m s⁻¹) westerly jet. The equatorially symmetric SST cases differ only in that cyclonic gyres occur on both sides of the jet. In all cases the rainfall is maximal at the east end of the jet. All the disturbances move to the east at speeds less than 10 m s⁻¹. This means that the jet speed is faster than the propagation speed of the disturbance.

The structure of the low-level flow closely resembles the composite MJO structure shown by Hendon and Salby (1994), and the eastward propagation speeds of the modes in the cases with an equatorial SST maximum are comparable to those exhibited by the observed MJO. The periodic eruption of convection over the warm pool and its subsequent eastward propagation and dissipation are also characteristic of the MJO, though the simulated repetition period of 27 d is at the low end of the usually quoted 30 - 60 d range of periods for the MJO.

Given the close resemblance of the simulated disturbance to the observed MJO, we

tentatively conclude that the simulations are capturing the essence of this phenomenon. The task now is to understand the mechanisms operating in the simulated disturbances. If observations reveal that these mechanisms are operating in the real world as well, it would bring us much closer to understanding this elusive phenomenon.

4 Analysis

We now analyze the above simulations and present the results of some auxiliary calculations with the purpose of understanding the physical mechanisms underlying the results.

4.1 Effective stability

Emanuel, Neelin, and Bretherton (1994) discussed the notion of effective static stability, pointing out that one effect of latent heat release is to diminish the negative buoyancy associated with large-scale vertical ascent. This reduces the horizontal propagation speeds of large-scale gravity waves. However, these authors didn't consider the possibility that the effective static stability could actually be *negative*.

Figure 11 shows the effective static stability for the simulation with uniform SST. The effective static stability is defined

$$\Gamma_{eff}(z) = \frac{\partial\theta}{\partial z} - \frac{\partial S_\theta}{\partial w} \quad (7)$$

where θ is the potential temperature, S_θ is the potential temperature source produced by the diabatic parameterizations, and w is the explicitly computed vertical velocity in the model. The value of $\partial S_\theta/\partial w$ is estimated as follows: At each level we fit a straight line to a scatter plot of S_θ vs. w for all grid points in a specified sub-domain of the numerical solution. The slope of this line is taken as the estimate of $\partial S_\theta/\partial w$.

As figure 11 indicates, the effective static stability computed for all grid points within 3000 km of the equator in the last 5000 ks of this simulation is actually negative between elevations 1.5 km and 8 km. This means that the large-scale behavior of the tropical

atmosphere in the model is not intrinsically wavelike. Rather, it has the character of large-scale convective overturning. This is a somewhat different picture of tropical disturbances than presented by Emanuel, Neelin, and Bretherton (1994), and in most other models of the tropical atmosphere.

Where does this large-scale convective instability come from? Two possible sources of the heating anomalies required to produce this instability are anomalies in surface latent and sensible heat fluxes (Emanuel's WISHE mechanism; Emanuel, 1993), and anomalies in radiative cooling caused by cloud-radiation interactions. The sum of these two anomalies (expressed as deviations from radiative-convective equilibrium) are responsible for driving the vertically integrated equivalent potential temperature budget, and thus possibly controlling the precipitation rate (Neelin and Held, 1987; Raymond, 2000b).

Forcing the surface total heat flux to be spatially uniform results in an equatorially symmetric wavenumber-two disturbance that moves to the east at about 3 m s^{-1} (results not shown). This disturbance is weaker than in the control case with uniform SST, but it does not decay. On the other hand, turning off cloud-radiation interactions results in no amplifying disturbances at all. Thus, cloud-radiation interactions are essential elements in the development of the modeled disturbance in the uniform SST case.

In order to develop a better understanding of this situation, a series of simpler two-dimensional simulations on an f -plane was undertaken. The Coriolis parameter was set uniformly to the value which occurs 1500 km north of the equator and the horizontal domain was 10000 km with rigid wall boundary conditions at the ends. The SST was fixed and disturbances were initiated with a humidity anomaly in the center of the domain plus a uniformly distributed random component. In all other respects these simulations were identical to the three-dimensional simulations discussed above.

As figure 12 shows, the initial humidity anomaly produces two weak traveling disturbances as it decays. The traveling disturbances move away from the initial anomaly at about $\pm 4 \text{ m s}^{-1}$, and decay when they encounter the domain boundaries. This case will be used later to illustrate other points. However, the main issue here is that the

existence of the traveling disturbances is sensitive to values of the cloud physics parameters in the diabatic parameterizations. In particular, altering the evaporation rate and the convective mixing velocity in various ways can either enhance or suppress the traveling disturbances. The details of these changes are not important here — the significant point is that all amplifying cases exhibited $\Gamma_{eff} < 0$ in some tropospheric layer at time $t = 50$ ks, while those in which the traveling disturbances decayed did not. The correlation between the sign of Γ_{eff} and the growth of disturbances in these simulations is further evidence that the growing modes in the present model are in essence radiative-convective instabilities.

4.2 Balanced dynamics

The relatively slow motion of the simulated disturbances suggests that some form of balanced dynamics is operating in these simulations. Sobel, Nilsson, and Polvani (2001) proposed a balanced dynamical theory appropriate to the tropics. (See also Sobel and Bretherton, 2000.) In their theory the temperature distribution on isobaric surfaces is assumed to be essentially constant above the boundary layer, as is generally observed in the deep tropics. This is thought to be brought about by the tendency of gravity waves to redistribute buoyancy anomalies over a very large area.

A consequence of this theory is that adiabatic cooling in ascent is almost completely balanced by heating due to latent heat release, radiation, and surface fluxes. Thus, knowledge of the heating immediately yields a good approximation to the vertical motion, which allows the divergence term in the vorticity equation to be evaluated. The evolution of the vorticity is thus well predicted as long as the heating is known, as is the pattern of divergence. From the vorticity and the divergence the velocity field can be calculated. To close the problem, one must determine the heating and moisture source terms.

The heating within active convection is mostly caused by latent heat release, and thus is closely related to the production of precipitation. The hypothesis of Raymond (2000b) relates the inverse of the precipitation rate to the mean saturation deficit of

the atmosphere, expressed in terms of the difference between the equivalent potential temperature and its saturation value:

$$\overline{\Delta\theta_e} \equiv \overline{\theta_{es}} - \overline{\theta_e} \propto (\text{precip rate})^{-1}. \quad (8)$$

The overbar indicates a density-weighted average through the troposphere. Figure 13 shows that this assumption is approximately valid in the numerical model results for the uniform SST simulation. Similar results hold for a wide variety of simulations with the model.

The final piece of the puzzle is provided by the governing equation for the equivalent potential temperature. Aside from the usual advection terms, this includes vertical redistribution due to convection as well as source and sink terms due to surface heat fluxes and radiation. (Irreversible generation of equivalent potential temperature, which occurs in the real atmosphere, is not included in the model thermodynamics.) In the absence of strong horizontal advection, the evolution of the vertically averaged θ_e is normally a slow process. This endows the atmosphere with a “moisture memory” of typically several days — the time it takes for the vertically integrated saturation deficit to respond significantly to surface fluxes and radiation. The evolution of rainfall rates is slow as well, with the exception of very moist atmospheres where the rainfall rate is a rapidly changing function of saturation deficit. As a result, the precipitation rate is not tightly coupled to surface heat fluxes in the present model. This is illustrated in figure 14, which shows a scatter plot of the net precipitation rate (precipitation minus evaporation) as a function of surface evaporation rate for the uniform SST case.

In contrast, certain other treatments of cumulus convection such as that provided by the Betts-Miller parameterization (Betts, 1986; Betts and Miller, 1986, 1993) exhibit very different behavior. Since excess precipitable water beyond that existing in a target humidity profile is precipitated out by a short-time-scale relaxation process, the dependence of precipitation rate on saturation deficit is much steeper in the Betts-Miller scheme than in ours. This is illustrated schematically in figure 13. As a consequence, models incorporating the Betts-Miller scheme exhibit a strict dependence between sur-

face evaporation and precipitation rate.¹ This behavior is illustrated by Sobel and Bretherton (2000) in the context of the Neelin-Zeng intermediate general circulation model (Neelin and Zeng, 2000; Zeng, Neelin, and Chou, 2000). As figure 2 in Sobel and Bretherton (2000) illustrates, this strict dependence is not found in observations, which are better mimicked by the results of the present model, as illustrated in figure 14.

The lag between enhanced surface fluxes and enhanced precipitation is a key feature in the dynamics of the present model. The two-dimensional model discussed briefly in the previous subsection illustrates the importance of this lag. As figure 12 shows, this simulation features two oppositely directed disturbances moving away from a common origin. Figure 15 shows that the rainfall maxima lag the maxima in surface heat flux by about 700 km, which corresponds to a time lag of about 2 d, given the propagation speeds of these disturbances. As the plot of saturation deficit shows, the period of strong surface fluxes corresponds to a time when the saturation deficit ahead of the peak rainfall is decreasing with time. Furthermore, as indicated earlier, the increase in rainfall nearly mirrors the decrease in saturation deficit. The net radiative cooling decreases to minimum values slightly in advance of the precipitation maxima, reflecting the fact that upper level winds blow the stratiform cloudiness out ahead of the disturbance in this case.

Comparison of figures 15 and 16 shows that the maxima in surface flux correspond to maxima in the low-level u wind, i. e., the wind component normal to the two-dimensional slab of the simulation. Furthermore, the low-level u wind is much stronger than the low-level v wind. As a consequence, the vorticity is much stronger than the divergence at low levels in this simulation.

In the sense of balanced dynamics, the vorticity “causes” the u wind, which is responsible for the enhanced surface fluxes. We can push the chain of causality further back by determining the cause of the vorticity maxima seen in figure 16. The origin

¹The relationship is not one-to-one, because precipitation originating from local evaporation causes heating and ascent, drawing in further water vapor from the environment which in turn precipitates out. Also, the strict dependence fails when the precipitable water is less than prescribed by the target humidity profile, since deep convection turns off in this case.

of the enhanced vorticity in this simulation is clearly the low level convergence associated with the ascent and rainfall occurring in these traveling disturbances. Since the enhanced rainfall is a consequence of the cloud-radiation interactions and the enhanced surface fluxes in our model, we have a closed loop explaining how these self-maintaining disturbances work:

$$\begin{aligned}
 & \text{precipitation} \Rightarrow \text{convergence} \Rightarrow \text{vorticity increase} \\
 & \Rightarrow \text{stronger balanced winds} \Rightarrow \text{enhanced surface fluxes} \\
 & \Rightarrow \text{decreased saturation deficit} \Rightarrow \text{more precipitation.} \tag{9}
 \end{aligned}$$

This is like Emanuel’s (1993) WISHE mechanism except that the wind anomaly is rotational rather than divergent in origin. However, in this case as well as in the three-dimensional simulations, no instability occurs if cloud-radiation interactions are not included as well. The resulting radiative heating anomalies are thus essential to the development of the simulated disturbances, and WISHE plays an important modifying role.

The disturbances simulated in the two-dimensional case are weak because the fetch over which fluxes act to reduce the saturation deficit is relatively small. This fetch is presumably related to the Rossby radius associated with the specified value of the Coriolis parameter. The three-dimensional disturbances exhibit a much larger fetch in a direction along the equator, and are correspondingly stronger. This is illustrated in figure 17 for the case of uniform SST. Furthermore, though the geometry is different, the propagation of these disturbances to the east can be explained by the principles summarized in (9) as well. In particular, the tendency to move to the east results from the fact that the most intense rainfall occurs at the east end of the westerly jet in each case, where the saturation deficit has decreased the most as the result of enhanced surface fluxes. This produces convergence, which spins up vorticity to the east of the existing vorticity maximum, thus causing this maximum to shift to the east. Something quite similar to this mechanism was proposed by Sobel, Nilsson, and Polvani (2001) in their recent work. As figure 18 shows, the westerly jet in the case of uniform SST is

primarily rotational in origin. The other three-dimensional cases are similar.

5 Conclusions

This paper presents a new model for the Madden-Julian oscillation. We draw the following conclusions from this work:

1. The deep tropics may actually be unstable to the vertical displacement of large scale parcels. This large-scale convective instability is made possible by cloud-radiation interactions. A pre-existing precipitation anomaly generally has a region of middle to upper level stratiform cloudiness associated with it. The suppression of outgoing longwave radiation results in a heating anomaly relative to its surroundings, which causes lifting and further precipitation.
2. The dynamics of the simulated disturbances can be understood in terms of the quasi-balanced model of Sobel, Nilsson, and Polvani (2001), in which heating interacts with the vorticity equation to produce flows which are predominantly solenoidal in certain critical regions. Surface heat flux anomalies resulting primarily from these solenoidal flows significantly modify the energy budget and behavior of the resulting disturbances. The modeling results confirm the above authors' assertion that slowly moving, quasi-balanced modes arise under these conditions.
3. The radiative-convective instability modes produced over a zonally symmetric equatorial SST maximum strongly resemble the MJO. Modes of wavenumber 1 move to the east at about 5 m s^{-1} . The important structural components of these modes are large, low-level cyclonic gyres on one or both sides of the equator coupled to a strong low-level westerly jet near the equator. The most intense precipitation occurs at the east end of the jet. When an equatorial warm pool is imposed on the zonally symmetric SST distribution, convective outbreaks periodically develop over the warm pool, move eastward, and dissipate. These outbreaks have a structure and movement similar to the disturbances which occur with zonally

symmetric SST.

4. The key condition in the model which makes these modes possible is a smooth inverse relationship between tropospheric saturation deficit and precipitation rate. This creates a situation in which the development of heavy precipitation can lag by several days the onset of enhanced surface fluxes. Thus, the heaviest precipitation need not occur where the surface fluxes are strongest.

At least two of the above assertions constitute testable hypotheses. First, it should be possible to determine to what extent observed westerly jets in the equatorial regions are balanced in the sense that they are primarily solenoidal flows derivable from the vorticity field. Second, the assertion that the precipitation rate in the deep tropics is primarily a function of the saturation deficit should be testable. If these assertions withstand inspection, then the present work should lead to a significantly better understanding of the MJO.

Acknowledgments. Thanks go to NOAA's Climate Diagnostics Center for providing the OLR data via their Web site. Discussions with George Kiladis significantly stimulated my thinking regarding the MJO, as did comments from Kerry Emanuel and Adam Sobel. The model was written in the SISAL language from Lawrence Livermore National Laboratory and the graphics were made with Dan Kelley's GRI package. This work was supported by National Science Foundation Grants ATM-9616290 and ATM-9983188, and NOAA Office of Global Programs Grant NA56GP0219.

6 References

- Betts, A. K., 1986: A new convective adjustment scheme. Part I: Observational and theoretical basis. *Quart. J. Roy. Meteor. Soc.*, **112**, 677-691.
- Betts, A. K., and M. J. Miller, 1986: A new convective adjustment scheme. Part II: Single column tests using GATE wave, BOMEX, ATEX and arctic air-mass data sets. *Quart. J. Roy. Meteor. Soc.*, **112**, 693-709.

- Betts, A. K., and M. J. Miller, 1993: *The Betts-Miller scheme*. The representation of cumulus convection in numerical models, AMS Monograph No. 46, 107-121.
- Emanuel, K., 1993: The effect of convective response time on WISHE modes. *J. Atmos. Sci.*, **50**, 1763-1775.
- Emanuel, K. A., J. D. Neelin, and C. S. Bretherton, 1994: On large-scale circulations in convecting atmospheres. *Quart. J. Roy. Meteor. Soc.*, **120**, 1111-1143.
- Emanuel, K. A., and D. J. Raymond, eds., 1993: The representation of cumulus convection in numerical models. AMS Monograph No. 46, 246 pp.
- Hayashi, Y., and D. G. Golder, 1993: Tropical 40-50 and 25-30 day oscillations appearing in realistic and idealized GFDL climate models and the ECMWF dataset. *J. Atmos. Sci.*, **50**, 464-494.
- Hendon, H. H., 1988: A simple model of the 40-50 day oscillation. *J. Atmos. Sci.*, **45**, 569-584.
- Hendon, H. H., and M. L. Salby, 1994: The life cycle of the Madden-Julian oscillation. *J. Atmos. Sci.*, **51**, 2225-2237.
- Johnson, R. H., and P. E. Ciesielski, 2000: Rainfall and radiative heating rates from TOGA COARE atmospheric budgets. *J. Atmos. Sci.*, **57**, 1497-1514.
- Lau, K.-M., T. Nakazawa, and C. H. Sui, 1991: Observations of cloud cluster hierarchies over the tropical western Pacific. *J. Geophys. Res.*, **96**, 3197-3208.
- Liebmann, B., and C. A. Smith, 1996: Description of a complete (interpolated) outgoing longwave radiation dataset. *Bull. Am. Meteor. Soc.*, **77**, 1275-1277.
- Lindzen, R. S., 1967: Planetary waves on beta-planes. *Mon. Wea. Rev.*, **95**, 441-451.
- Madden, R., and P. R. Julian, 1971: Detection of a 40-50 day oscillation in the zonal wind in the tropical Pacific. *J. Atmos. Sci.*, **28**, 702-708.

- Madden, R., and P. R. Julian, 1972: Description of global-scale circulation cells in the tropics with a 40-50 day period. *J. Atmos. Sci.*, **29**, 1109-1123.
- Madden, R. A., and P. R. Julian, 1994: Observations of the 40-50 day tropical oscillation — a review. *Mon. Wea. Rev.*, **122**, 814-837.
- Matsuno, T., 1966: Quasi-geostrophic motions in the equatorial area. *J. Meteor. Soc. Japan*, **44**, 25-43.
- Moskowitz, B. M., and C. S. Bretherton, 2000: An analysis of frictional feedback on a moist equatorial Kelvin mode. *J. Atmos. Sci.*, **57**, 2188-2206.
- Neelin, J. D., and I. M. Held, 1987: Modeling tropical convergence based on the moist static energy budget. *Mon. Wea. Rev.*, **115**, 3-12.
- Neelin, J. D., and N. Zeng, 2000: A quasi-equilibrium tropical circulation model — formulation. *J. Atmos. Sci.*, **57**, 1741-1766.
- Peixoto, J. P., and A. H. Oort, 1992: *Physics of climate*. American Institute of Physics, 520 pp.
- Randall, D. A., Harshvardhan, D. A. Dazlich, and T. G. Corsetti, 1989: Interactions among radiation, convection, and large-scale dynamics in a general circulation model. *J. Atmos. Sci.*, **46**, 1943-1970.
- Raymond, D. J., 1994: Convective processes and tropical atmospheric circulations. *Quart. J. Roy. Meteor. Soc.*, **120**, 1431-1455.
- Raymond, D. J., 1995: Regulation of moist convection over the west Pacific warm pool. *J. Atmos. Sci.*, **52**, 3945-3959.
- Raymond, D. J., 2000: The Hadley circulation as a radiative-convective instability. *J. Atmos. Sci.*, **57**, 1286-1297.
- Raymond, D. J., 2000: Thermodynamic control of tropical rainfall. *Quart. J. Roy. Meteor. Soc.*, **126**, 889-898.

- Raymond, D. J., and D. J. Torres, 1998: Fundamental moist modes of the equatorial troposphere. *J. Atmos. Sci.*, **55**, 1771-1790.
- Raymond, D. J., and X. Zeng, 2000: Instability and large-scale circulations in a two-column model of the tropical troposphere. *Quart. J. Roy. Meteor. Soc.*, **126**, 3117-3135.
- Salby, M. L., R. R. Garcia, and H. H. Hendon, 1994: Planetary-scale circulations in the presence of climatological and wave-induced heating. *J. Atmos. Sci.*, **51**, 2344-2367.
- Salby, M. L., and H. H. Hendon, 1994: Intraseasonal behavior of clouds, temperature, and motion in the tropics. *J. Atmos. Sci.*, **51**, 2207-2224.
- Sherwood, S. C., V. Ramanathan, T. P. Barnett, M. K. Tyree, and E. Roeckner, 1994: Response of an atmospheric general circulation model to radiative forcing of tropical clouds. *J. Geophys. Res.*, **99**, 20829-20845.
- Slingo, A., and J. M. Slingo, 1988: The response of a general circulation model to cloud longwave radiative forcing. I: Introduction and initial experiments. *Quart. J. Roy. Meteor. Soc.*, **114**, 1027-1062.
- Slingo, J. M., and A. Slingo, 1991: The response of a general circulation model to cloud longwave radiative forcing. II: Further studies. *Quart. J. Roy. Meteor. Soc.*, **117**, 333-364.
- Smith, R. K., ed., 1997: The physics and parameterization of moist atmospheric convection. Kluwer, 498 pp.
- Sobel, A. H., and C. S. Bretherton, 2000: Modeling tropical precipitation in a single column. *J. Climate*, **13**, 4378-4392.
- Sobel, A. H., J. Nilsson, and L. M. Polvani, 2001: The weak temperature gradient approximation, and balanced tropical moisture waves. *J. Atmos. Sci.*, (in revision).

Wang, B., and H. Rui, 1990: Dynamics of the coupled moist Kelvin-Rossby wave on an equatorial beta plane. *J. Atmos. Sci.*, **47**, 397-413.

Wheeler, M., and G. N. Kiladis, 1999: Convectively coupled equatorial waves: Analysis of clouds and temperature in the wavenumber-frequency domain. *J. Atmos. Sci.*, **56**, 374-399.

Zeng, N., J. D. Neelin, and C. Chou, 2000: A quasi-equilibrium tropical circulation model – implementation and simulation. *J. Atmos. Sci.*, **57**, 1767-1796.

Figures

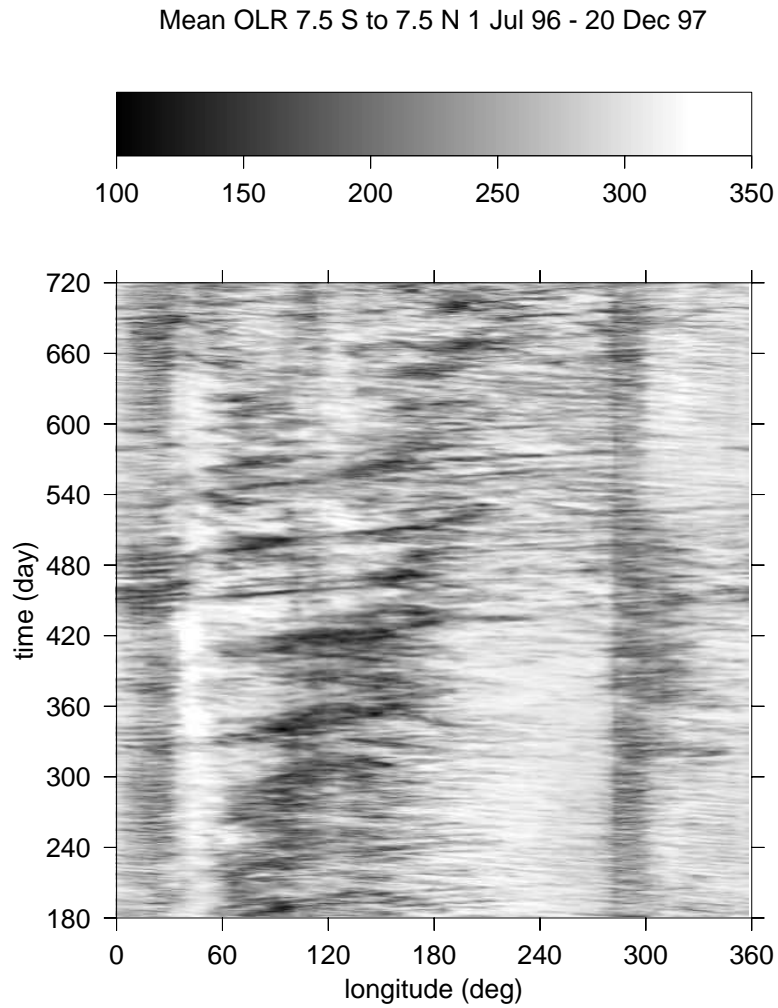


Figure 1: Unfiltered daily OLR averaged over the latitude range 7.5° S to 7.5° N for the period 1 July 1996 to 20 December 1997. West longitudes are represented by their equivalent east longitude values. Gray scale limits range from 100 W m^{-2} (black) to 325 W m^{-2} (white).

Mean OLR 7.5 N to 12.5 N 1 Jul 96 - 20 Dec 97

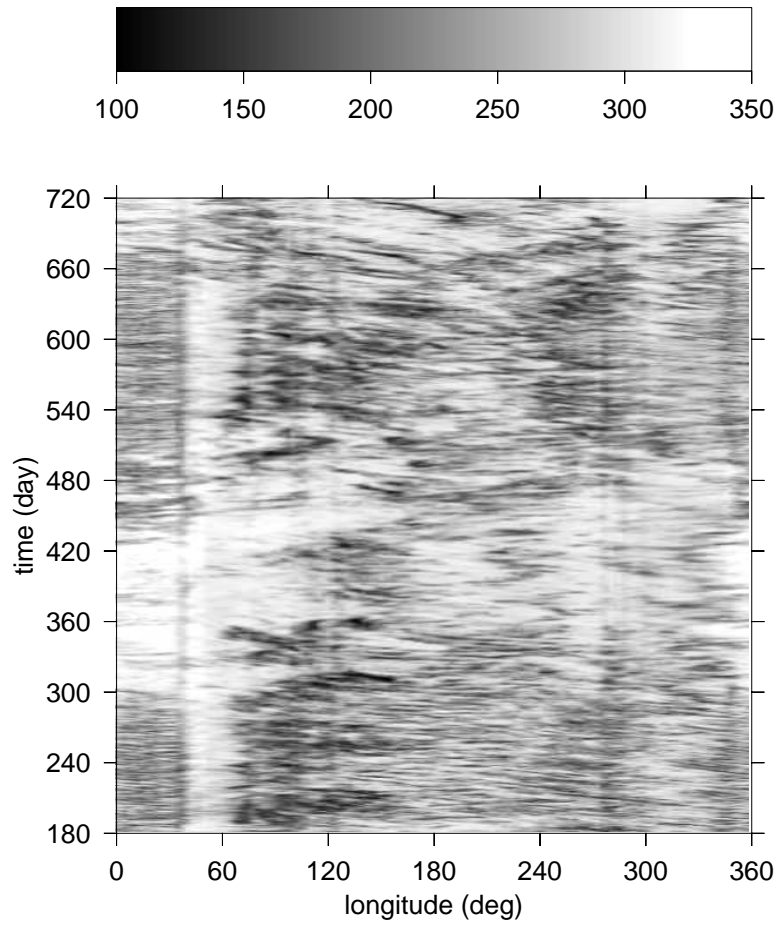


Figure 2: As in figure 1 except latitude range 7.5° N to 12.5° N.

Mean OLR 12.5 S to 7.5 S 1 Jul 96 - 20 Dec 97

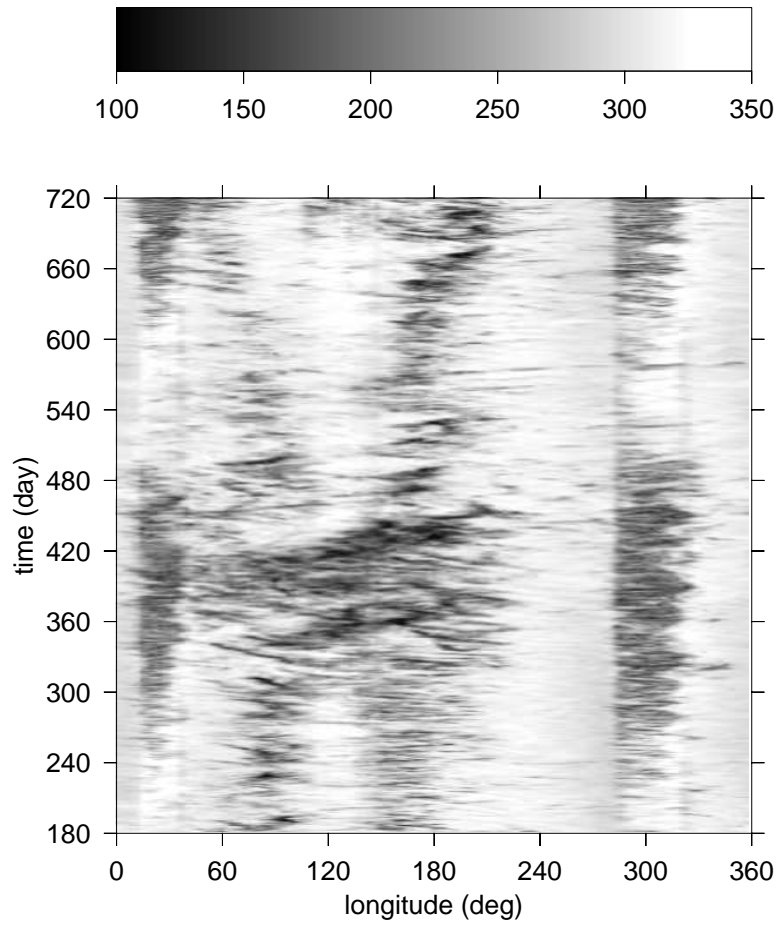


Figure 3: As in figure 1 except latitude range 12.5° S to 7.5° S.

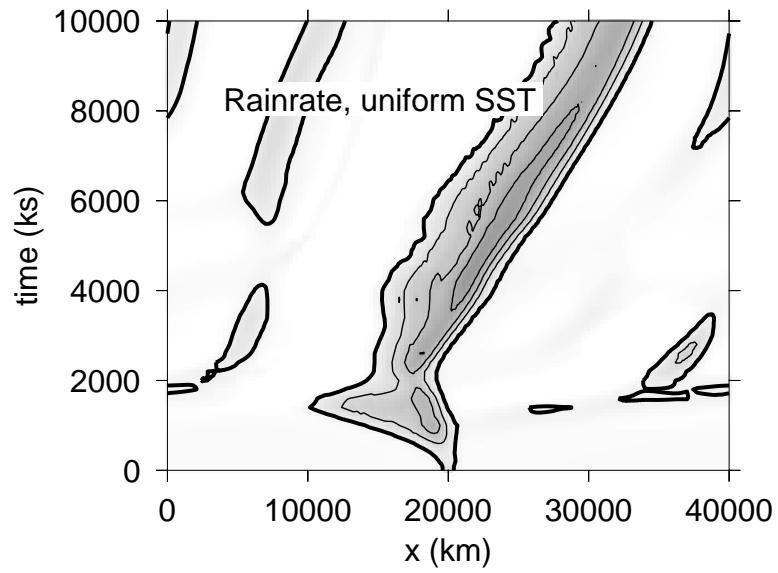


Figure 4: Rainfall rate as a function of longitude and time at $y = 5750$ km (750 km north of the equator) for the flat SST case. The contour interval is 5 mm d^{-1} and the 5 mm d^{-1} contour is indicated by a thicker line.

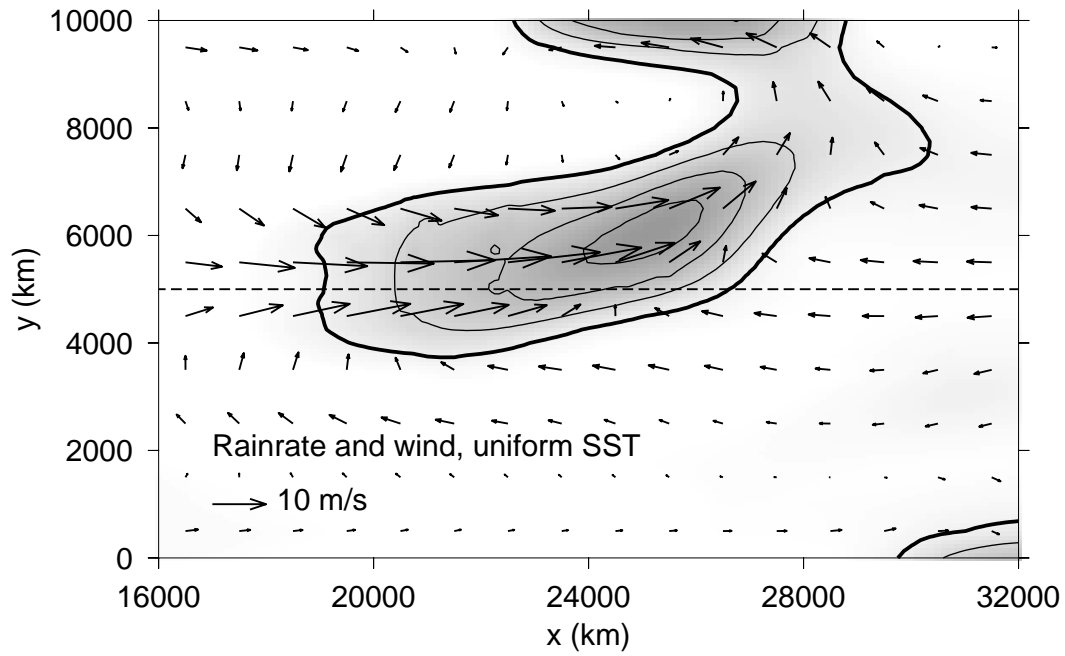


Figure 5: Rainfall rate (contours and gray scale) and mean winds averaged over the lowest 4 km at $t = 6000$ ks for the flat SST case. The contour interval on rainfall rate is 5 mm d^{-1} . The 5 mm d^{-1} contour line is thicker than the other contours. The dashed line indicates the equator. Only a subset of the x domain is shown.

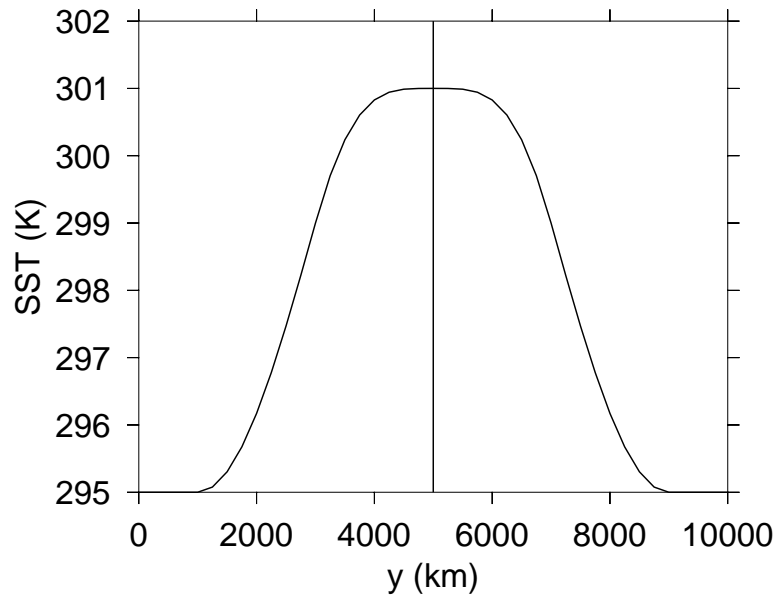


Figure 6: Meridional SST distribution for zonally symmetric SST calculation. The vertical line indicates the equator.

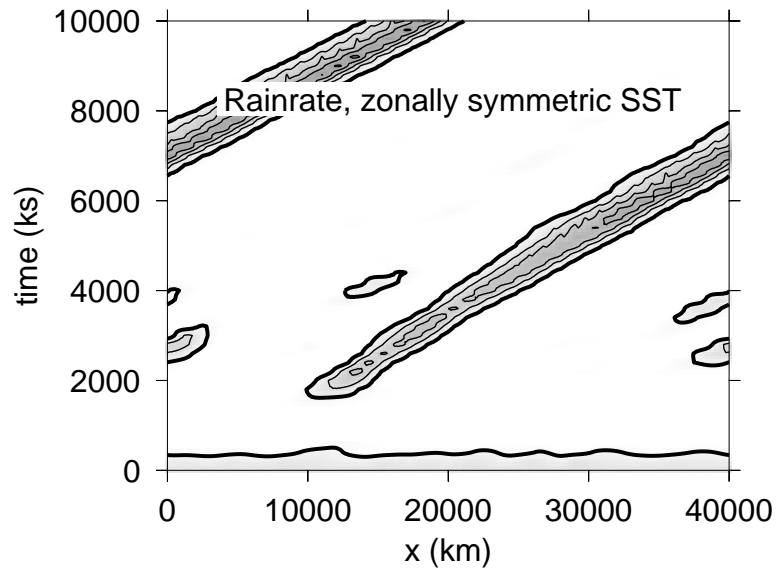


Figure 7: As in figure 4 except at $y = 5000$ km, i. e., on the equator, for zonally symmetric SST distribution.

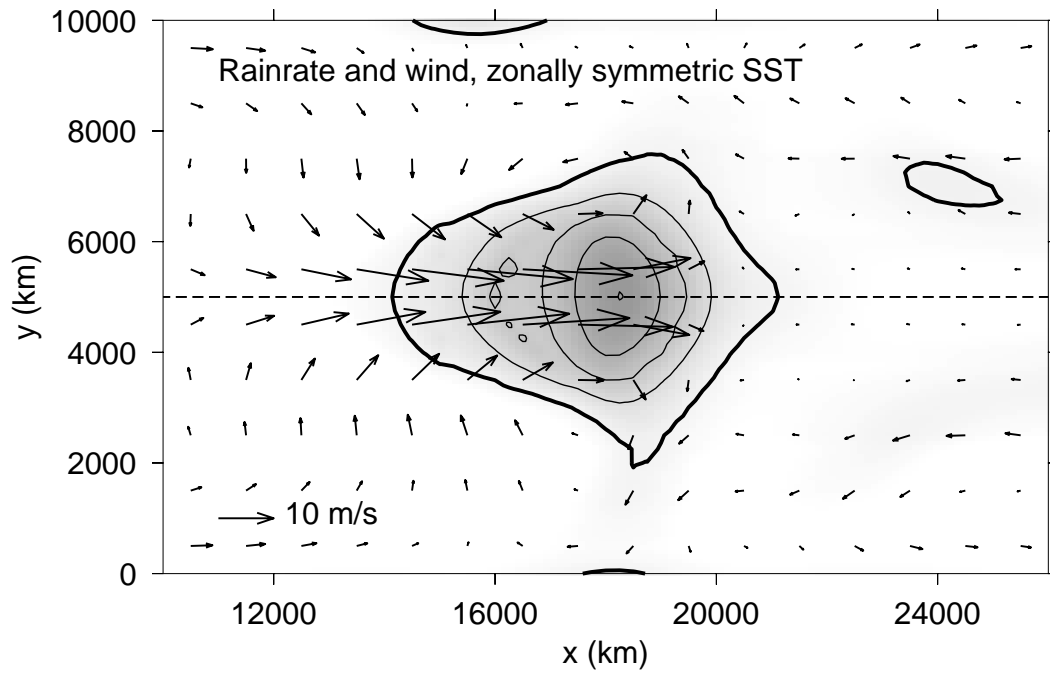


Figure 8: As in figure 5 except for case of zonally symmetric SST distribution with an equatorial maximum at time $t = 10000$ ks.

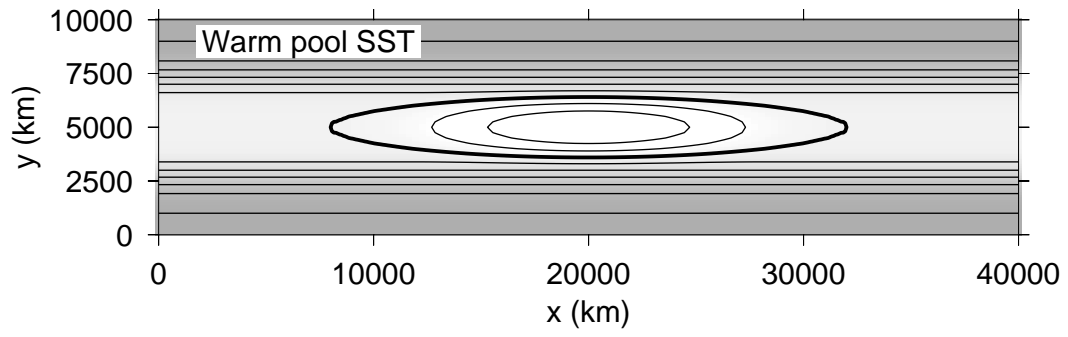


Figure 9: SST distribution for the warm pool calculation. The contour interval is 1 K and the 301 K contour is thicker than the others.

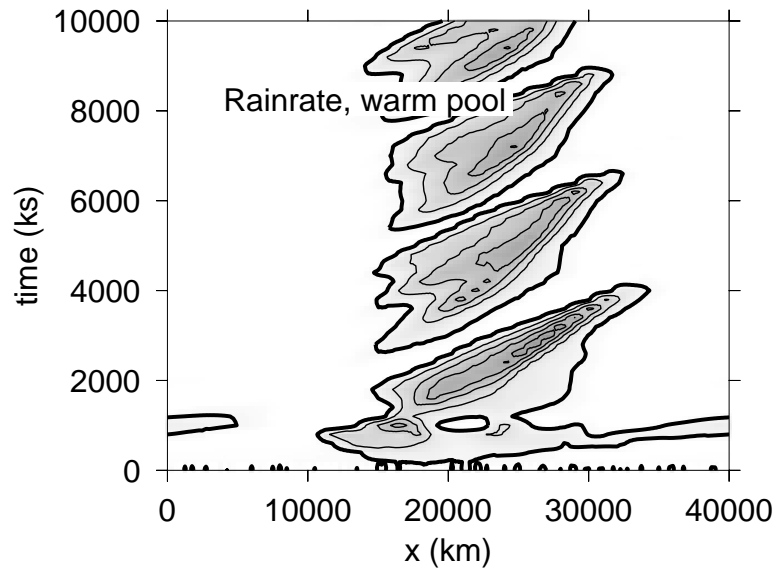


Figure 10: As in figure 4 except for the warm pool SST distribution, with the data slice taken at $y = 5000$ km, i. e., on the equator.

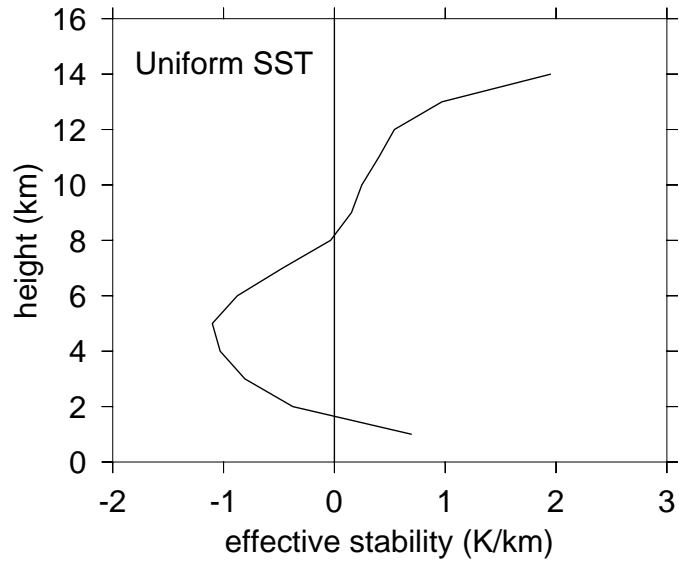


Figure 11: Effective static stability, $\Gamma_{eff}(z)$, for the case of uniform SST. Only gridpoints within 3000 km of the equator in the last 5000 ks of the simulation are included in the computation.

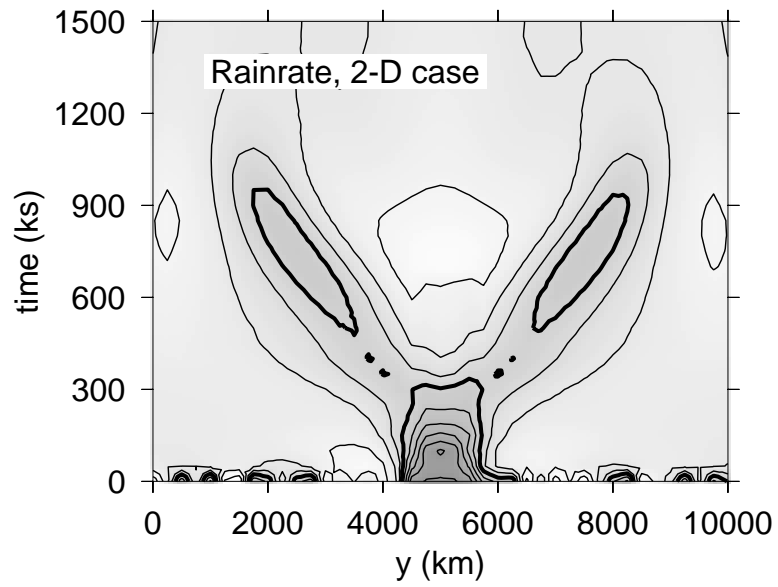


Figure 12: As in figure 4 except two-dimensional case, with a contour interval of 1 mm d^{-1} .



Figure 13: Scatter plot of mean saturation deficit vs. rainfall rate for the uniform SST simulation. The corresponding relationship for the Betts-Miller cumulus parameterization is schematically illustrated by the steep diagonal line.

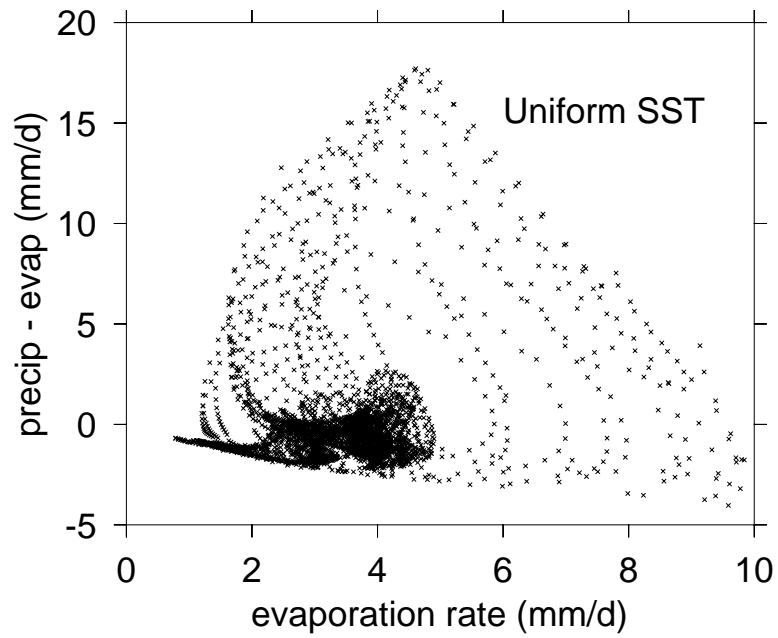


Figure 14: Scatter plot of net rainfall rate (rainfall minus evaporation) vs. evaporation rate for the uniform SST case. Only points within 3000 km of the equator are shown.

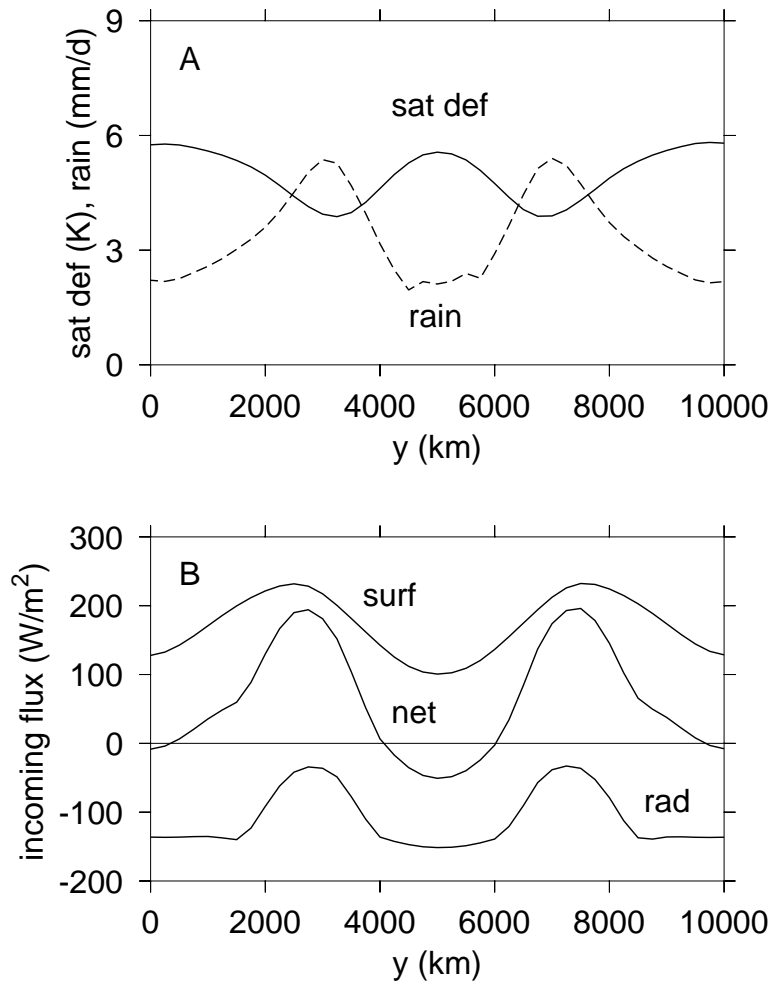


Figure 15: Thermodynamic characteristics of the two-dimensional simulation of figure 12 at $t = 600$ ks. (a) Mean saturation deficit and rainfall rate. (b) Surface sensible plus latent heat flux, integrated radiative cooling rate, and the sum of these two fluxes.

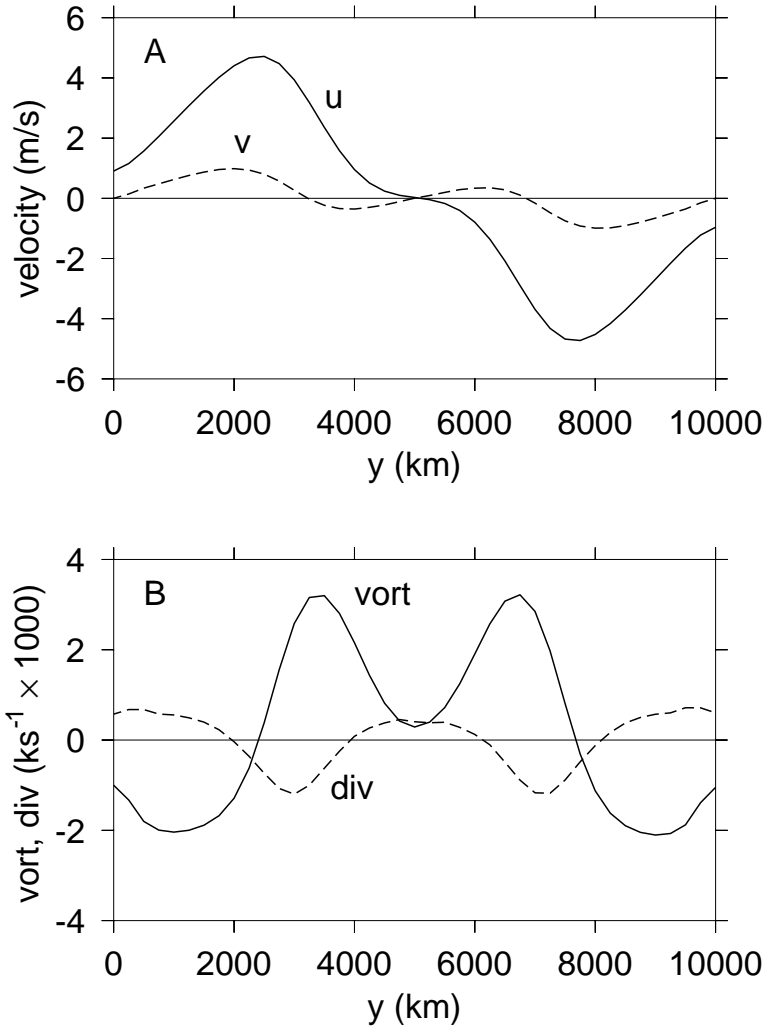


Figure 16: Dynamic characteristics of the two-dimensional simulation of figure 12 at $t = 600$ ks. (a) Horizontal wind components (u normal to the plane of symmetry, v in the plane) averaged over the lowest 4 km. (b) Vorticity and divergence derived from u and v respectively.

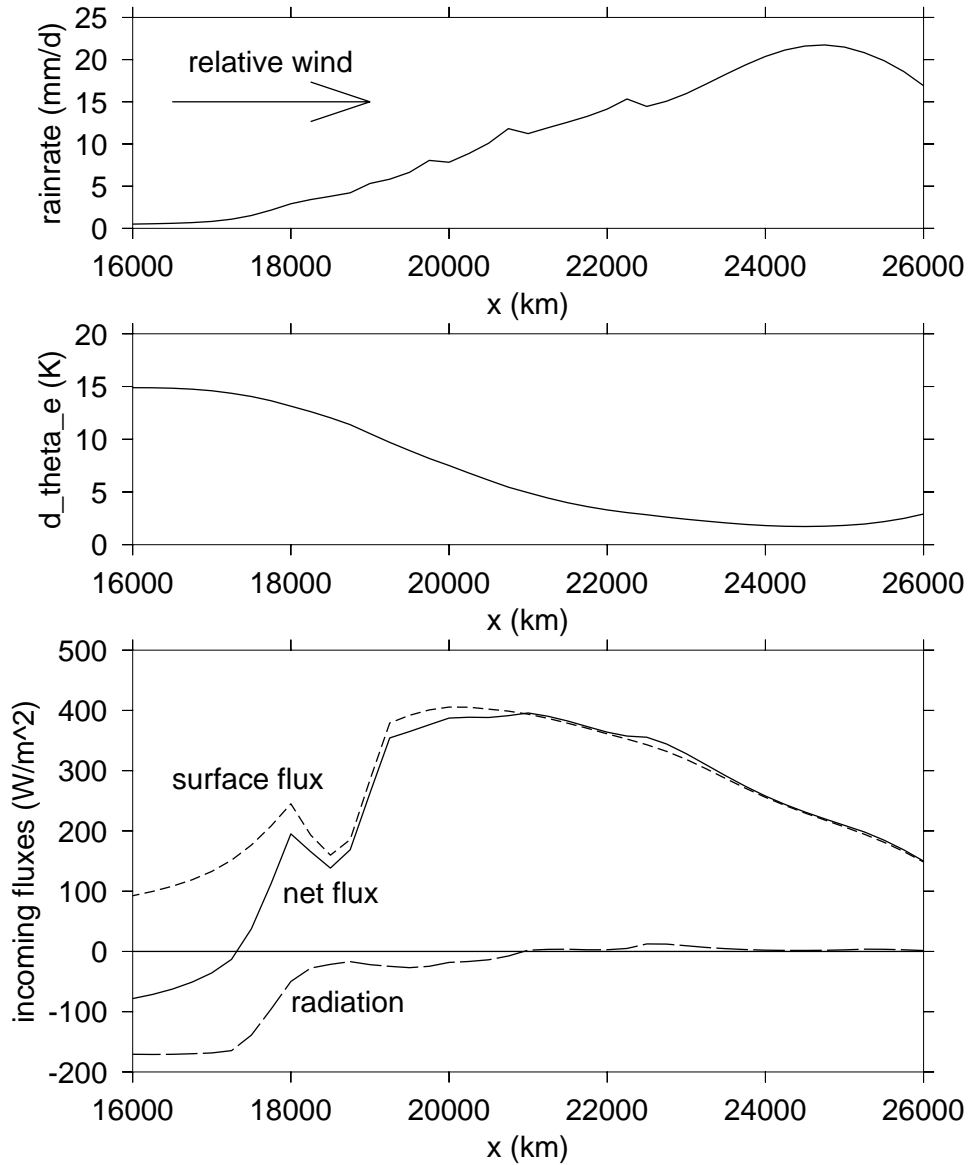


Figure 17: Section of westerly jet between $x = 16000$ km and $x = 26000$ km along $y = 5750$ km at time $t = 6000$ ks for the case of uniform SST. The upper panel shows the rainfall rate, the middle panel shows $\Delta\theta_e$ averaged over the lowest 4 km, and the bottom panel shows the latent plus sensible surface heat flux, the total radiative flux entering the atmosphere, and their sum, the net flux.

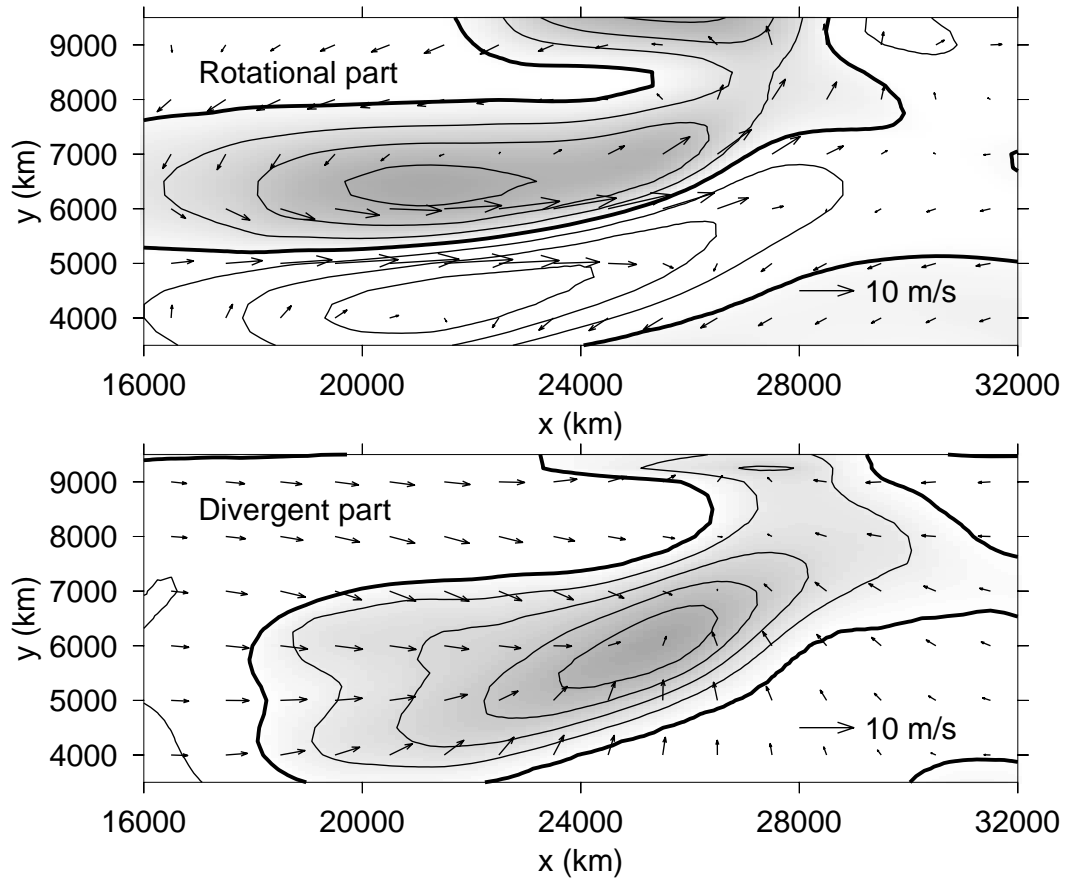


Figure 18: Division of the westerly wind burst shown in figure 5 into rotational (upper panel) and divergent (lower panel) parts. The relative vorticity is shown in the upper panel (contours and shading) with a contour interval of $4 \times 10^{-3} \text{ ks}^{-1}$. The divergence is similarly shown in the lower panel with a contour interval of $1 \times 10^{-3} \text{ ks}^{-1}$. Positive vorticity is dark, while negative divergence is dark. In both cases the zero contour is thicker.